



Research Paper

Metal 3D-printed wick structures for heat pipe application: Capillary performance analysis

Davoud Jafari^{a,*}, Wessel W. Wits^a, Bernard J. Geurts^b^a Faculty of Engineering Technology, University of Twente, P.O. Box 217, 7500 AE Enschede, The Netherlands^b Faculty of Electrical Engineering, Mathematics and Computer Science, University of Twente, P.O. Box 217, 7500 AE Enschede, The Netherlands

HIGHLIGHTS

- Capillary performance of a metal 3D-printed porous structure is evaluated.
- Effects of working fluids on the capillary pumping of 3D-printed wicks are studied.
- The computed pressure drop of the sample is compared with the available models.
- Gravitational effect on the capillary pumping of 3D-printed wicks is determined.
- Capillary performance of 3D-printed wicks is compared to conventional wicks.

ARTICLE INFO

Keywords:

Heat pipe
Porous structure
Additive manufacturing
Permeability
Capillary performance

ABSTRACT

This paper examines the so-called capillary performance of a freeform porous structure fabricated by advanced 3D metal printing technology. The fabricated structure is intended as wick for two-phase heat transfer devices, in which it contributes to the transport of a liquid working fluid through capillary forces. A stainless steel porous structure is additively manufactured and characterized in terms of its porosity (ϵ), effective pore radius (r_{eff}), liquid permeability (K) and capillary performance (K/r_{eff}). Forced liquid flow tests with deionized water as working fluid are conducted to determine the permeability. Capillary penetration experiments are performed by means of height-time (h - t) and weight-time (w - t) techniques with different fluids to characterize the capillary performance of the printed wicks. The experimentally determined values of permeability and pressure drop are compared with the well-known Darcy's law and Forchheimer corrections. The Kozeny–Carman correlation is found to predict the experimental values of permeability at lower flow velocities (0.07 m/s corresponding to a Reynolds number of 0.95), while at higher velocities an under-prediction of the experimental data is observed. The Kozeny-like model taking into account inertial effects is updated in terms of constant values that fit with the experimental data very well. The accuracy of the theoretical models for characterizing capillary rate-or-rise processes is also assessed. It is concluded that the capillary penetration of liquids in the 3D-printed wick follows the law: $h(t) \sim t^{1/3}$ at intermediate stage. Observation confirms that the gravitational effect played a significant role in the 3D-printed wick, introducing slower capillary rising. Compared to sintered powder, screen mesh and composite wicks selected from literature, the designed 3D-printed wick enhances the capillary performance. It is concluded that due to the large permeability and capillary performance (K/r_{eff}), heat pipes in conjunction with a 3D-printed wick can significantly augment their heat transfer.

1. Introduction

Two-phase passive heat transfer devices enjoy strongly increasing attention, because of their importance for industrial thermal management problems [1–5], building upon their effective and reliable performance. Heat pipes, as passive heat transfer devices, operate by utilizing the latent heat of an internal working fluid [6,7]. Porous

structures are at the heart of heat pipes. They are utilized as capillary-wicking medium to drive the circulation of working fluid in its liquid phase, as well as evaporation-enhancement structures to release/capture the working fluid in its vapor phase. In heat pipe design, wick performance is often a limiting factor [8]. Common homogeneous wicks for heat pipes are made of grooves [9,10], wrapped screens [11] or sintered metal solutions [12,13]. Such homogenous shapes stem from

* Corresponding author.

E-mail addresses: j.davoud@yahoo.com, davoud.jafari@utwente.nl (D. Jafari).<https://doi.org/10.1016/j.applthermaleng.2018.07.111>

Received 19 May 2018; Received in revised form 17 July 2018; Accepted 22 July 2018

Available online 24 July 2018

1359-4311/ © 2018 The Authors. Published by Elsevier Ltd. This is an open access article under the CC BY-NC-ND license (<http://creativecommons.org/licenses/by-nc-nd/4.0/>).

manufacturing constraints and influence the wick's performance. For the performance of a wick, the capillary pressure it may generate and its permeability to the working fluid are key indicators. Ideally, one requires structures that generate high capillary pressure, combined with high permeability. Current solutions do not fully realize this. For instance, a screen wick generates a moderate capillary pressure at low permeability [14–16]. The performance of axial grooved wicks is quite good in terms of its permeability [17], while the low capillary pumping pressure of such wicks severely limits applications in case the working fluid must ascent against gravity. The permeability of sintered wicks is generally low, because small pores of the sintered porous wick cause a large pressure drop in the liquid-flow passage [16]. Recently, much research [18–27] is devoted to more advanced composite wicks including composite screens and screen-covered grooves. These solutions provide high-capillary pressure and high permeability, but also require complex manufacturing steps. With current advances in metal 3D printing, an additively manufactured porous wick structure could well be an alternative, offering small-scale feature sizes and 3D ligament arrangements in a variety of possible configurations. In this case, 3D printing allows much greater freedom in defining the wick geometry and properties – in this paper, we therefore investigate experimentally the wick quality with potential use in heat pipes in mind.

Unlike conventional manufacturing processes, additive manufacturing (AM), colloquially known as 3D printing, can directly produce complex 3D parts [28,29]. It is a process whereby a solid object is fabricated directly from the digital CAD file. Especially, metal powder bed fusion technologies, such as selective laser melting (SLM), offer the possibility to combine solid and porous regions within one part. The main benefit of a 3D-printed wick is in the fabrication of a freeform porous structure with complex geometry and optimized internal pore structure, which can be integrated flexibly without introducing further interfaces, as a single manufactured heat pipe. This will result in a significant improvement of the rate with which heat can be removed, potentially, leading to an important breakthrough in thermal management systems.

Recently, 3D-printed wicks have been proposed to fabricate predefined net-shape porous structures such as open-cellular stochastic foams and reticulated meshes [30] and hexagonal lattices [31]. Research specifically aimed at 3D printing porous structures for two-phase heat transfer devices is scarce. Very recently, Jafari and Wits [32] reviewed advanced heat transfer devices utilizing additive manufacturing. Esarte et al. [33] presented a 3D-printed wick for loop heat pipes. The wick was characterized for permeability, capillary pumping and thermal conductivity, and showed a 10% increase in heat transfer rate compared to a conventional solution. Ameli et al. [34] reported on 3D-printing of an aluminium wick structure for heat pipes with ammonia as the working fluid. Randomized and regular porous structures were tested. Recently, Jafari et al. [35] fabricated and tested a stainless steel porous structure for heat pipe applications utilizing SLM. They showed that the effective thermal conductivity of the particular 3D-printed wick is in the range of 3 W/m·K for ethylene glycol and 6 W/m·K for water as tested working fluids, thereby establishing a high sensitivity of the thermal conductivity to the interstitial fluid.

Although a large body of literature is devoted to permeability [36–39] and capillary performance [40–42] evaluation of packed bed powder, sintered powder wicks and composite porous structures, 3D-printed wick structures have been barely investigated thus far. In this study, an experimental set-up is developed to perform analyses of single-phase heat transfer properties of a 3D-printed stainless steel wick using various working fluids. Several key performance parameters for the wick structure, affecting the heat transfer performance and capillary limit of a heat pipe are characterized: porosity, effective pore radius, permeability, capillary pumping performance and wettability. Forced liquid flow tests are performed to evaluate the permeability of the wick. Furthermore, the rate-of-rise test of liquid in a porous structure is used to characterize the wick capillary performance. Liquid uptake is

determined by both mass and wetted height. Prior to the capillary penetration experiments, the porous structure was characterized using scanning electron microscopy (SEM). Finally, the capillary performance of an SLM-fabricated porous structure is compared to available wicks for heat pipe applications as reported earlier in the literature. This paper is organized as follows. The hydraulic performance description of porous structures is described in Section 2, followed by presenting the experimental facilities in Section 3. Subsequently, Section 4 addresses a discussion of results including permeability measurement and capillary rise tests. Concluding remarks are presented in Section 5.

2. Hydraulic performance description of proposed 3D printing of porous structures for two-phase heat transfer devices: Theoretical models

In heat pipe applications, there are several key performance parameters for the wick structure which determine the ultimate heat transfer performance: permeability and capillarity, among others. The permeability is a measure for the openness of the structure, and hence, for the effort needed to transport the liquid working fluid through the wick and the capillarity is a measure for the pumping power of the wick, by which the working fluid can be transported through the system. The ratio K/r_{eff} is a key parameter, characterizing the capillary limit of a wick for heat pipe devices and is often referred to as the capillary performance [43]. Here, K is the permeability of the porous structure and r_{eff} is the effective pore radius. r_{eff} is a parameter used to describe the pressure rise for liquid pumping. r_{eff} is defined as $r_p/\cos\theta$ where r_p is the pore radius and θ is the contact angle of the working fluid with the wick material.

The permeability and pressure drop in porous structures depend on several parameters such as the porosity, pore size and its distribution. Increasing K and decreasing r_{eff} are key design issues for enhancing the liquid propagation rate. A small pore size of a wick leads to low effective pore radius of the wick and high capillary pressure, but it also decreases the permeability. Therefore, it is essential to estimate conflicting properties when designing wick structures for heat pipe devices: permeability (K), effective pore radius (r_{eff}), and also K/r_{eff} as a single parameter which captures the trade-off between the former two competing and conflicting properties. In this section, theory behind the development of an experimental setup, suitable to accurately characterize the hydraulic performance of a 3D-printed wick is presented.

2.1. Theoretical model and research objective: Permeability

Permeability is commonly measured in forced flow tests using liquid or gas, during which the achieved flow rate is recorded upon imposing a prescribed pressure drop. For liquid flow in wicks, in case of water, when the velocity is sufficiently small, inertial effects are negligible and the permeability of a wick is determined by Darcy's law [6,16]. The well-known Darcy's law states that the pressure drop (ΔP) across the porous medium per unit length (L) is proportional to the effective fluid velocity (v), the dynamic viscosity (μ), and inversely proportional to the permeability coefficient (K):

$$\frac{\Delta P}{L} = \frac{\mu}{K} v \quad (1)$$

where the effective flow velocity given by $v = \dot{m}/\rho A$. Here, A is the average cross-sectional area of the wick, available to liquid flow. For higher flow velocities, > 0.1 m/s [44], where drag becomes important, an approach based on Forchheimer corrections is used [18,45] to predict the pressure drop:

$$\frac{\Delta P}{L} = \underbrace{\frac{1}{K_1} \mu v}_{\text{Darcy term}} + \underbrace{\frac{1}{K_2} \rho v^2}_{\text{Forchheimer term}} \quad (2)$$

where K_1 is the Darcyan permeability coefficient and corresponding

constant ($1/K_1$) is the Darcy term (m^{-2}), K_2 is non-Darcyan permeability coefficient and the corresponding constant ($1/K_2$) is the Forchheimer term (m^{-1}) or so-called form drag coefficient. Since both Darcyan and non-Darcyan terms are affected by the structure of the wick, i.e. porosity, pore size, etc., it is necessary to evaluate and adopt the available predictable expression for permeability and pressure drop of a new porous media, herein 3D-printed wicks.

One should take into account when evaluating the hydraulic performance of porous structures is type of flow regime, particularly the Reynolds number. An important length scale, square root of permeability (\sqrt{K}) [46], can be used in the definition of the Reynolds number in the porous medium, which is called permeability-based Reynolds number (Re_K) [47]:

$$Re_K = \frac{\rho \sqrt{K} v}{\mu} \quad (3)$$

The value for K can be calculated by two different approaches: (i) using the permeability obtained from pressure drop and flow velocity values up to which the transition takes place based on expression (1), K ; (ii) using larger flow velocity values, obtained from Forchheimer correction (2), K_1 . Based on above mentioned Reynolds number, distinct flow regimes are recognized, namely: Darcy flow regime ($Re_K < 1$), Forchheimer flow regime ($1 < Re_K < 150$), and post-Forchheimer flow regime and fully turbulent flow ($Re_K > 150$) [47]. By systematically varying the pressure drop over a sample, and recording the average flow velocity that arises, one may readily extract K , K_1 and K_2 from the observed data.

2.2. Theoretical models and research objective: Capillary performance

The capillary rate-of-rise test can be used to characterize the capillary performance parameters of a wick structure, i.e., K/r_{eff} [42,48]. The capillary rate-of-rise test consists of dipping a sample in a reservoir containing liquid and measuring (i) the wetted height above the level of the reservoir as a function of time (height-time technique, $h-t$) and/or (ii) the measurement of the increase in weight of the sample caused by the liquid penetration as a function of time until the capillary and hydrostatic pressures equilibrate [6,43].

For the rise of liquid in a wick with small effective pore diameters (approximately $< 300 \mu m$ for water), three pressures are assumed to be in balance at the wetted height. Capillary pressure (ΔP_c) is assumed to be in balance with the hydrostatic pressure (ΔP_h) and the pressure loss associated with friction (ΔP_f), neglecting momentum [14]:

$$\Delta P_c = \frac{2\sigma \cos\theta}{r_p} \quad (4)$$

$$\Delta P_h = \rho g h \quad (5)$$

$$\Delta P_f = \frac{\mu \varepsilon}{K} h \frac{dh}{dt} \quad (6)$$

where σ is the liquid surface tension, g is the gravitational acceleration, ε is the porosity of the sample and dh/dt is the capillary rise velocity. In order to characterize a wick, the cosine of the contact angle (θ) of the working fluid with the wick material is usually set to unity assuming good wettability. As mentioned before, the pore radius (r_p) is replaced by the effective capillary radius ($r_{eff} = r_p/\cos\theta$). This implies:

$$\Delta P_c = \frac{2\sigma}{r_{eff}} \quad (7)$$

Therefore, according to momentum balance ($\Delta P_c = \Delta P_f + \Delta P_h$) at the wetted height of the sample:

$$\underbrace{\frac{2\sigma}{r_{eff}}}_{\text{capillary pressure}} = \underbrace{\frac{\mu \varepsilon}{K} h \frac{dh}{dt}}_{\text{viscous term}} + \underbrace{\rho g h}_{\text{gravity term}} \quad (8)$$

To evaluate the capillary performance when gravity effects cannot be neglected, Eq. (8) can be rewritten including the parameter K/r_{eff} as:

$$\frac{dh}{dt} = \frac{2\sigma}{\mu \varepsilon} \frac{K}{r_{eff}} \frac{1}{h} - \frac{\rho g K}{\mu \varepsilon} \quad (9)$$

In this case, capillary performance can be determined by the capillary rise height ($x = 1/h$) and capillary rise velocity ($y = dh/dt$) assuming working fluid properties and wick porosity are known as:

$$y = \frac{2\sigma}{\mu \varepsilon} \frac{K}{r_{eff}} x - \frac{\rho g K}{\mu \varepsilon} \quad (10)$$

If gravity is negligible, Eq. (8) reduces to the Washburn's equation. In this approach, it is assumed that only displacement changes with time, therefore:

$$\frac{K}{r_{eff}} = \frac{\mu \varepsilon}{4\sigma} \frac{h^2}{t} \quad (11)$$

In Eq. (11), there is a linear relation between h^2 and t as long as the assumptions (no inertia, no gravity) hold.

The relation between the height of the liquid and the capillary pumping mass is:

$$h = \frac{m}{\rho \varepsilon A} \quad (12)$$

Hence, mass (m) and capillary rise mass (dm/dt) can be determined when gravity effects cannot be neglected and squared mass (m^2) versus time can be computed neglecting gravity effect as well.

Considerable studies on capillary fluid uptake by porous structures have been reported on the basis of the fundamental study of Washburn ($h-t^{1/2}$) [49]. However, the accuracy of this formulation is insufficient in some cases and researchers have reported contradicting results from this method [50–56]. $w-t$ and $h-t$ techniques have been also compared for silica gel powders [57,58] and for polyethylene porous media and cellulose paper in [59] and discrepancies were reported due to porous media properties (e.g., porosity and pore sizes distribution) and wetting liquid (i.e., viscosity and surface tension) [60].

Based on the above discussion, though considerable studies indicated that the capillary performance can be generally evaluated by the classical Washburn expression in which the rise of height (or mass) is proportional to the square root of time ($h(t)$ or $w(t) \sim t^{1/2}$). Neglected by the Washburn model, the gravitational effect may influence the capillary rise. Ponomarenko et al. [61] observed that the normalized capillary rise height is proportional to the cubic root of time

$$\frac{h(t)}{a} \left(\frac{\sigma t}{\mu a} \right)^{1/3} \quad (13)$$

where $a = (\sigma/\rho g)^{1/2}$ is the capillary length. The contact angle characterizing the wetting of the liquid on the solid is assumed to be completely wetting. This expression will also be evaluated in this paper to characterize the capillary rise dynamics of a 3D-printed wick. Deng et al. [62] experimentally showed that the capillary rise in a groove wick first follows the Washburn relation, $h(t) \sim t^{1/2}$, and then is governed by the $h(t) \sim t^{1/3}$.

In the case of a 3D-printed wick, the determination of the wicking height is difficult, but by measuring weight as a function of time, visualizing the rising fluid front and image processing can be avoided. The $w-t$ technique however features some disadvantages when compared to the $h-t$ technique. As the sample in this study, has a small thickness (1 mm) compared to the width (20 mm), the initial effect of wetting is the attachment of an outer meniscus to the wick, may result in a significant rise in mass when compared to the mass gain due to the wicking effect alone as was reported in [63]. For this reason, the measurement and comparison of both liquid height and weight as a function of time will determine whether these techniques are applicable in capillary-wicking structures fabricated by 3D printing. The capillary

Table 1
Specifications of metal powder used for metal 3D printing.

Metal powder	
Commercial name	CL 20ES
Material	Stainless steel, chemical composition according to CrNiMo 17% 13% 2%, 316L
Shape	Irregular
Particle size: average/minimum/maximum	33/7.8/53.9 (μm)
Thermal conductivity	0.15 (W/m·K)

rise mass can be computed relatively easy by a precise balance, while different imaging techniques exist to visualize the height of the fluid front: e.g. recording images during the capillary rise [64–66] and InfraRed (IR) thermography [67]. Due to the difference in emissivity of the working fluid and the wick material, the rise of the meniscus can be recorded through IR [56]. In this paper, an IR thermal imaging method is utilized to evaluate the capillary rise height

3. Development of experimental setup

3.1. Porous sample and its characterization using SEM

Specifications of the metal powder employed for fabricating of the porous structure are summarised in Table 1. The selected powder has a fine average particle size, according to SEM image provided in Fig. 1(a). The powder material size distribution is presented in Fig. 1(b). It has a

Table 2
Specifications of selective laser melting process.

SLM machine	Concept Laser Mlab Cusing 90
Laser system	yttrium fiber laser 100 W, wavelength: 1.07 μm
Laser scan speed	7 m/s
Laser focus diameter	40 μm
Layer thickness	50 μm
Hatch distance	1.3 mm
Protective gas	Nitrogen

particle size range of 7.8–53.9 μm , an average of 33 μm .

A 3D-printed porous structure of $1 \times 20 \times 40 \text{ mm}^3$ is manufactured from the metal powder by SLM using an Mlab Cusing 90, 3D Metal Printing machine. Specifications of the SLM machine are given in Table 2. An Yttrium fiber laser is employed with maximum laser output of 100 W at a wavelength of 1.07 μm . Fabrication is achieved in layers. Each layer is added by first depositing the powder feedstock on the already printed structure to a thickness of 50 μm . The laser beam is then employed and scanned over the surface with a nominal beam diameter of 40 μm . After printing one layer, a next layer of powder is added for subsequent printing. The power and exposure time of the laser during each layer are set to control the degree of melting of the powder. This exposure time defines the pore size of the porous structure as minimum feature size and hence determines the porosity. A nitrogen atmosphere is used to prevent oxidation of the metal powder during manufacturing. The manufactured structure is finally removed from the substrate plate using a wire erosion process to avoid excessive smearing of the pores.

The sample is generated by formation of 3D octahedral unit cells

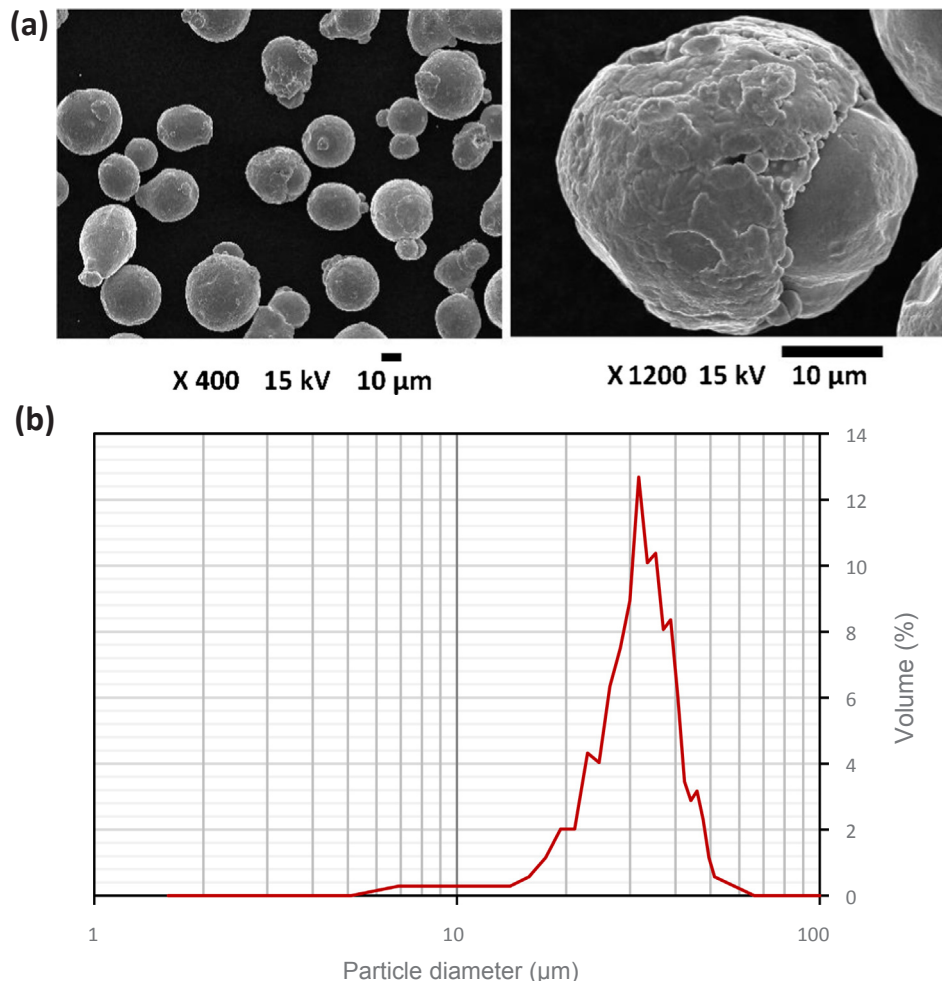


Fig. 1. (a) SEM image of feedstock powder and (b) its particle size distribution.

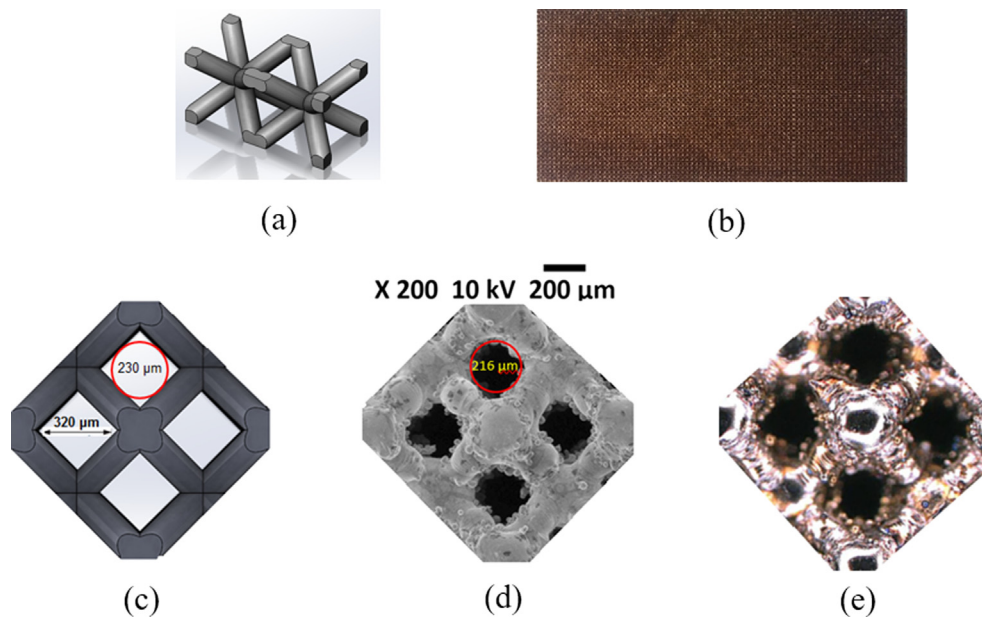


Fig. 2. 3D-printed stainless steel wick: (a) Unit cell, (b) a photo of the 3D-printed sample of $1 \times 20 \times 40 \text{ mm}^3$, (c) proposed CAD model, (d) SEM image and (e) optical microscopic image.

with sides of $500 \mu\text{m}$. Fig. 2 shows the unit cell, the proposed CAD model of the sample, SEM image of the sample as well as a photo of the final part. The minimum, maximum and average dimensions of pore sizes are characterized from several cross-section images (see Table 1), following the tool described in [68]. One of the main advantages of 3D printing is that it allows producing porous structures with a controlled geometry. In this study, the mean pore size of the 3D-printed produced wick ($216 \mu\text{m}$) is about 6% lower than as designed in the CAD file ($230 \mu\text{m}$).

3.2. Porosity measurement

For measuring the porosity of the fabricated sample, a balance is used to weigh the sample before and after saturating it with methanol. Methanol is used rather than, for example, water, due to its volatility. The porosity is measured by weighing the amount of methanol required to saturate the wick following the Archimedes method:

$$\frac{1}{\varepsilon} = 1 + \frac{m_p \rho_l}{m_l \rho_p} \quad (14)$$

where ε is the porosity, m_p and m_l are the porous structure and methanol liquid masses, respectively, and ρ_p and ρ_l are the metal powder and methanol mass densities, respectively. To ensure a complete saturation of the sample, a dry sample is placed on a balance. The fluid is delivered to the wick until the wick is flooded. The fluid evaporates and at the point when the surface of the methanol recedes below the pores, the weight is noted. A precise balance is used to measure weight. Repeated trials indicated a deviation of less than 2% variation in the porosity values. The average porosity of the tested sample is 0.46.

3.3. Permeability measurement using forced flow

A linear pressure drop test facility is used to determine the permeability of porous structure using the forced liquid flow method as shown in Fig. 3. The set-up is manufactured from acrylic, and consists of a flow housing, a cover plate, the test sample and sealing components. An O-ring is used, preventing any flow on the top side of the sample. A good sealing is maintained by clamping all the test components together. The top cover plate is precisely positioned to prevent compression of the wick sample. The liquid flow, degassed water, is forced through the

sample by sending pressurized nitrogen gas to a water tank to provide a broad range of smooth mass flow rates.

The test sample is cleaned prior to insertion into the test section, following the procedure described in [69]. The cleaning process involves immersing the sample in a solution of nitric acid and hydrofluoric acid. This is followed by placing the sample in an electric furnace and heating in air to 400°C for 1 h. Once the sealed test section connects to the flow loop, liquid is passed through the test chamber at varying mass flow rates. A pressure transducer is installed in the inlet flow to measure the inlet pressure. The pressure at the outlet is the atmospheric pressure. After the test section, water is collected in a container and placed on a balance. Measured mass change data is collected for 120 s and used to compute the mass flow rate for each test. The flow rate is measured at steady state. Water was flushed through the sample for 10 min before beginning the measurements to remove any air bubbles trapped in the sample. To check for constancy of the flow rate, three successive measurements of flow rate are performed for each test.

3.4. Capillary rate-of-rise test

The set-up to perform a rising meniscus test is shown in Fig. 4. The experiment takes place in a glass chamber to minimize evaporation of liquid during the entire capillary rise process. The experimental assembly consists of an analytical balance from which the porous sample is suspended in a vertical position. The sample hangs above a platform that holds a liquid bath. To perform a measurement, the precision lifting table is used to lift the liquid and bring it into contact with the porous sample. The balance measures a change in weight as liquid is drawn into the porous structure. The balance is interfaced to a computer and the weight is recorded continuously as a function of time. Water, methanol, *n*-Hexane and FC-72 are used as fluids.

Simultaneously, height measurements of the liquid meniscus are recorded. An IR camera is used to accurately identify the front location based on the difference in emissivity of the liquid and sample material. In such a way, the meniscus is identified and recorded as a function of time. Methanol and *n*-Hexane are used as fluids for the *h-t* technique.

The container of liquid is cleaned for each type of liquid. Furthermore, a standard cleaning protocol for stainless steel porous structures is performed prior to all tests [69]. Three sets of experiments

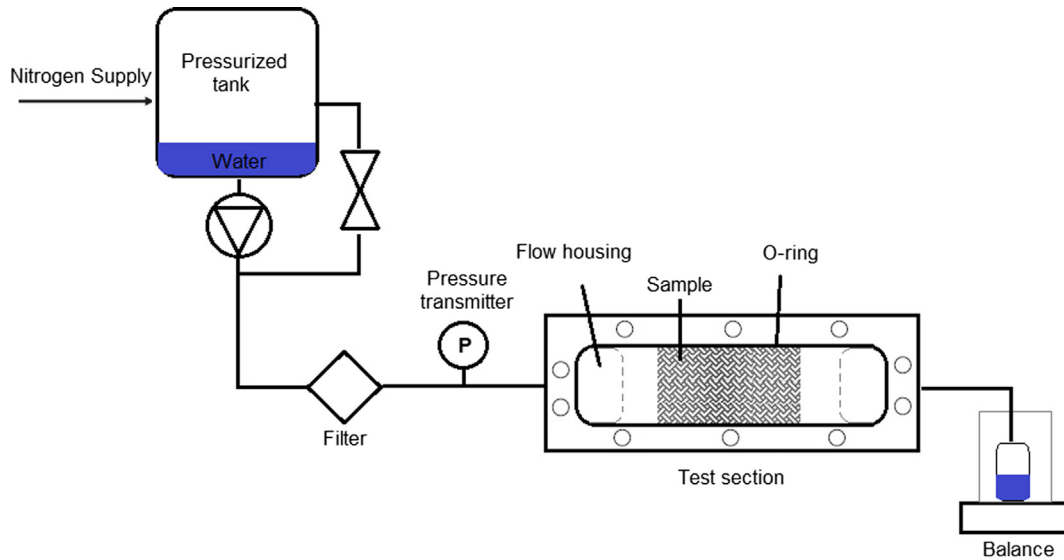


Fig. 3. Forced liquid flow set-up to measure permeability of a 3D-printed porous structure.

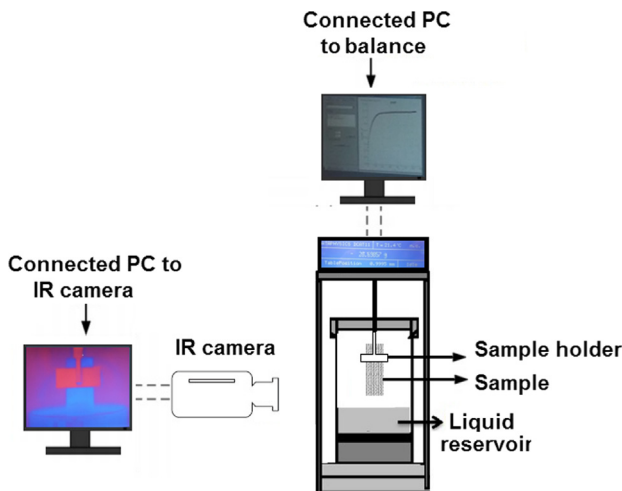


Fig. 4. Experimental set-up used for the capillary penetration tests of a 3D-printed porous structure.

were performed for each type of liquid to make sure the data was reproducible. The experiments ended when the weight became constant and the sample was saturated (or the liquid reached an equilibrium height).

3.5. Uncertainty analysis

Using a standard error analysis method [70], the root of the sum of the squares method, the measurement uncertainty was computed. The measurement uncertainty for the electronic balance was in the range of 10^{-4} g. The uncertainty measurement of mass was 0.38%. The uncertainty of the geometry was estimated at about ± 0.1 mm. The uncertainty of the porosity depends on the measurement uncertainty of mass and volume, calculated at 2.6%. The uncertainty of the permeability depends on the measurement uncertainty of the corresponding parameters (the length and the cross section of the wick sample, pressure drop and mass flow rate). The uncertainty analysis is performed based on a pressure transducer error of 86 Pa and a precise balance with a resolution of 10^{-4} g. In the capillary fluid uptake test, a Xenics IR Camera (Gobi 384) was used with a high thermal resolution of 0.05°C at 30°C to measure the wetted height while an electronic micro balance (DCAT 11, DataPhysics) with a precision of 10^{-5} g was used for mass

measurements. The maximum uncertainties associated with the capillary pumping force are computed as 6.2% and 4.6% for h - t and w - t techniques, respectively. Associated uncertainty of permeability values ranged from 8.5 to 10.4% and as each mass flow rate was tested three times, the associated standard deviation ranged from 2.4 to 6.8% which is within the uncertainty of permeability values.

4. Results and discussion

A 3D-printed wick is experimentally tested to evaluate its hydraulic characteristics. The characterization procedure involved determining two performance criteria: the permeability and capillary performance. For the first criterion, the pressure drop versus flow velocity behavior in the 3D-printed wick is evaluated in detail at different fluid velocities. The well-known Darcy's law and Forchheimer corrections are introduced to define the permeability of the sample. Furthermore, the transition from Darcy regime to Forchheimer regime is addressed based on the Re_K . The semi-empirical Kozeny–Carman equation, which is often used to determine the permeability of porous structures for heat pipes is presented and discussed. For the second criterion, capillary performance, the experimental results of capillary rate-of-rise tests employing w - t and h - t techniques are presented. The experimental data from these techniques are evaluated through the Washburn's equation, $h(t) \sim t^{1/2}$. The capillary rise dynamics of the sample is evaluated for different working fluids in term of $h/a \sim (\sigma t/\mu a)^{1/3}$ curves as well. Capillary performance of the wick is evaluated and compared in terms of K/r_{eff} for both w - t and h - t techniques. Finally, the wick properties and capillary performance of the fabricated 3D-printed wick of this study is compared to available porous structures for heat pipe devices in the literature.

4.1. Permeability measurement using forced flow

The permeability (K) of the sample is evaluated according to (1) using the described test facility and is summarized in Fig. 5. The experiments are performed at varying mass flow rates from ~ 0.4 to 4 g/s. It is immediately evidenced that the fluid flow velocity affects the permeability value. A relatively flat region of the permeability, located near the low end of the range, marks the linear pressure drop flow regime in which Darcy's law holds. The value of permeability reaches a relatively constant value of $K = 1.35 \times 10^{-10} \text{ m}^2$ at a maximum flow velocity of approximately 0.07 m/s (1.3 g/s). After this relatively constant value, the permeability decreases. A possible explanation for the

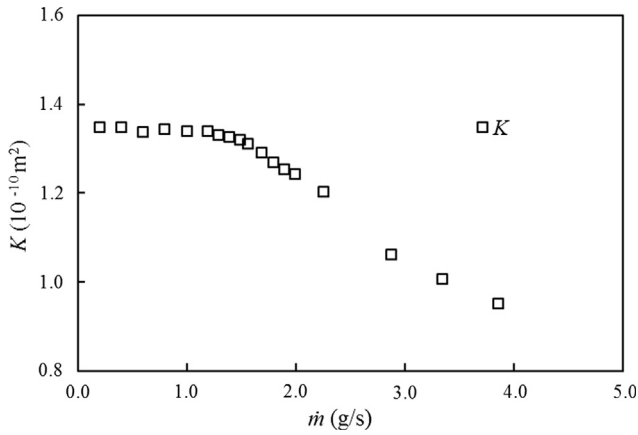


Fig. 5. Permeability (K) test results according to (1) for different mass flow rates (\dot{m}).

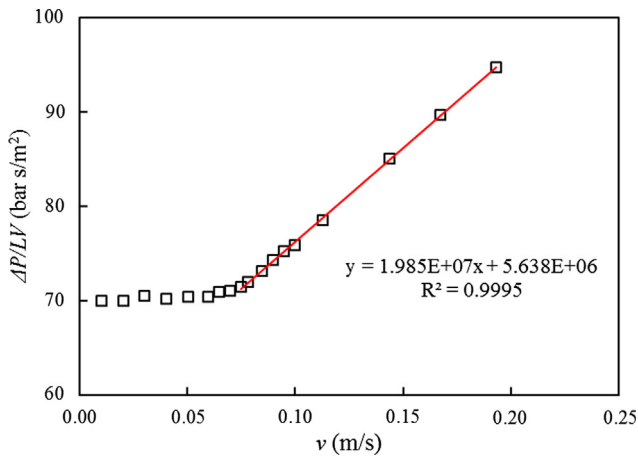


Fig. 6. Pressure drop divided by the wick length and fluid velocities versus fluid velocities as well as curve-fit constants according to (2).

constant permeability values and the following decreasing values is presented as follow. As the fluid velocity increases, the Darcy equation fails to describe the pressure drop behavior. A quadratic term, referred to as the Forchheimer or the form drag term, added to (1), captures the effect of the force exerted by any solid surface on the fluid flow and its resultant effect on the pressure drop, (2). Fig. 6 contains plots of the pressure drop divided by the wick length and fluid velocity versus fluid velocity. The pressure drop plotted according to this approach should be linear according to (2):

$$\frac{\Delta P}{Lv} = \alpha + \beta v \quad (15)$$

Coefficients α and β are μ/K_1 and ρ/K_2 , respectively. These values are used to calculate the Darcyan and non-Darcyan permeability constants K_1 and K_2 , respectively, at flow velocities above 0.07 m/s. Results are given in Table 3. The viscous contribution is characterized by K_1 taking into account the linear dependency with the flow rate. The

Table 3
Computed K , K_1 and K_2 according to (1) and (2).

Permeability constant		
Darcy permeability according to (1)	Forchheimer permeability coefficients according to (2)	
$K \text{ (m}^2\text{)}$	$K_1 \text{ (m}^2\text{)}$	$K_2 \text{ (m)}$
1.35×10^{-10}	1.67×10^{-10}	5.03×10^{-5}

inertial contribution is described by K_2 taking into account the quadratic dependence with the flow rate. The plotted line has a slope of β . When β is relatively equal to zero, it describes the pressure drop region where the constant, $1/K_2$, is near zero and the pressure drop is governed entirely by Darcy's law. Darcyan flow regime is indeed observed at flow speeds less than 0.07 m/s. At flow velocities higher than this transitional flow velocity value, the experimental data turns onto the fitted line with a non-zero slope of β . The permeability is determined at $1.67 \times 10^{-10} \text{ m}^2$, which is about 19.4% higher than the average permeability based on Darcy's law ($v < 0.07 \text{ m/s}$). The difference is due to the form drag term in Forchheimer correction. Table 3 summarizes the computed permeability coefficients according to the Darcyan and Forchheimer expressions. It can be concluded that in this case neglecting the Forchheimer term at flow velocities higher than 0.07 m/s leads to about 20% error for computing permeability of the wick structure.

To characterize Re_K , the values for permeability are computed according to (1) and (2): K and K_1 . The dimensionless pressure drop (ψ) versus the Reynolds number is considered for the transition regime evaluation [71]:

$$\psi = \frac{\Delta P}{L} \frac{D}{\rho v^2} \quad (16)$$

Fig. 7 shows the variation of ψ versus Re_K and Re_{K1} for the sample. It should be noted is that the relation between the normalized pressure drop and flow velocity is non-linear. Hence, it is important to determine when the pressure drop across the wick leaves the linear Darcy regime. By analysing the data according to Figs. 5 and 6, the transition takes place at a flow velocity of 0.07 m/s. This value corresponds to a Reynolds number of 0.95 which is almost identical to the Reynolds number of unity reported in the literature [47]. The corresponding error for computing Re_K neglecting the Forchheimer term at flow velocities higher than 0.07 m/s is about 12–29% from low to high velocities.

It is also important to compare the computed pressured drop values with the available models and expressions in the literature. Usually, satisfactory predictions can be obtained by Darcy's law, which lumps all complex interactions between the fluid and wick structure into permeability. In order to predict the permeability of a porous wick and to compare with the experimental data, the well-known Kozeny–Carman equation is widely used. For low Reynolds numbers ($Re_K < 1$), the Carman–Kozeny model, correlates permeability with porosity and pore size, according to:

$$\frac{\Delta P}{L} = C \frac{(1-\epsilon)^2}{D^2 \epsilon^3} \mu v \quad (17)$$

and for high Reynolds numbers to take into account inertial effects of the fluid, according to [72]

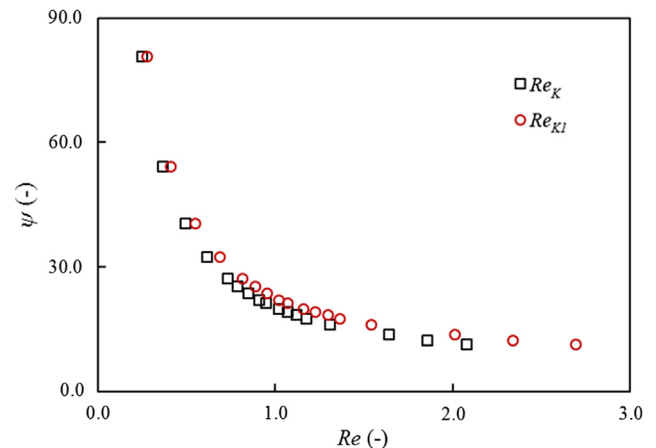


Fig. 7. Comparison of experimental dimensionless pressure drop (ψ) versus Reynolds number (Re_K and Re_{K1}).

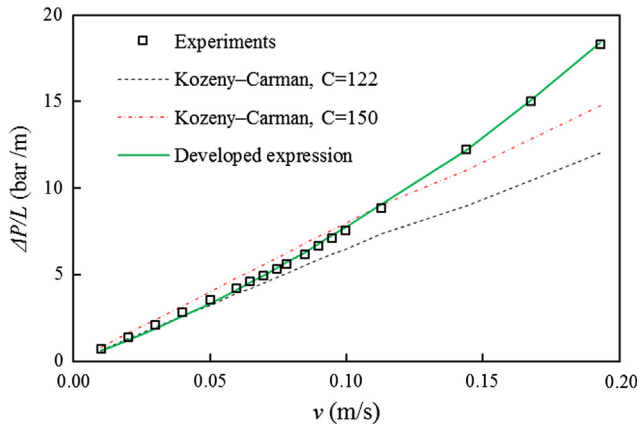


Fig. 8. Experimentally measured and predicted pressure drop from the literature.

$$\frac{\Delta P}{L} = a \frac{(1-\varepsilon)^2}{D^2 \varepsilon^3} \mu v + b \frac{1-\varepsilon}{D^2 \varepsilon^3} \rho v^2 \quad (18)$$

where C is a geometrical factor depending on properties of the wick structure, and $a = 150$ and $b = 1.75$ are the original values of coefficients [72]. The C factor is unknown and usually its value is determined experimentally. For a uniformly packed and a sintered porous media, C values are commonly 122 [73], 150 [14] and 180 [36] or other much larger values [39]. The difficulty with Kozeny-like models is that they are derived for packed-bed media. Thus, it cannot accurately represent the structure and flow through 3D-printed porous structures due to the notably complexity of the structure and its roughness. Fig. 8 shows a comparison between measured and predicted pressure drops per unit length as a function of liquid velocity. The plot shows an increase in the pressure drop with increasing liquid velocity, the variation between the actual values and the different correlations is quite considerable. The best agreement between measured and computed values is obtained with the correlation of Kozeny–Carman with a C value of 122 for low liquid velocities. However, at higher flow velocities, > 0.07 m/s ($Re_K = 0.95$), under-prediction of experimental data is observed. According to (18) as indicated by the solid line, approximations are obtained leading satisfactory correlation coefficients of $a = 105$ and $b = 0.9$.

Herein, we aim to relate the results of the presented data to design a 3D-printed wick for heat pipe devices. In a saturated wick for a heat pipe device, the liquid flow regime in the wick is assumed to be laminar, the momentum equations however can be extended to include the Darcy and Forchheimer. Based on the results of this study it is possible to state flow regimes and associated hydraulic characterization of a 3D-printed wick structure. It is found that the transition regime between the linear Darcy regime and when drag becomes important (Forchheimer corrections) for the tested sample occurs at $Re_K = 0.95$, which corresponds to a flow velocity of 0.07 m/s based on the calculation of the permeability and form coefficient in this range. Therefore, to design a 3D-printed wick, knowing the pore size and porosity, as well as estimating flow velocity ($v = q/\rho h_{fg}$, where v is the fluid velocity, q is the applied heat flux and h_{fg} is the latent heat of vaporization) through the heat pipe, the pressure drop can be obtained either by Darcyan or non-Darcyan flow regime depending the Reynolds number. It is concluded that \sqrt{K} is smaller than the pore diameter with an approximate order of magnitude ($10^{-3}D$): $K = 2.5 \times 10^{-3}D$ and $K_1 = 3.1 \times 10^{-3}D$. As in heat pipe devices, flow through porous structures is laminar and Darcy's law is usually applied the permeability of the tested sample is $1.35 \times 10^{-10} \text{ m}^2$ at a maximum flow velocity of approximately 0.07 m/s and Re_K of 0.95 . Bonnet et al. [74] showed that this expression valid for laminar flow. Paiva and Mantelli [18] experimentally and analytically evaluated a hybrid sintered metal powder

Table 4

Values of surface tension (σ), density (ρ) and dynamic viscosity (μ) of tested fluids and their capillary length: $Ca = (\sigma/\rho g)^{1/2}$.

Fluid	σ 10^{-3} (N/m)	ρ (kg/m ³)	μ 10^{-3} (Pa s)	Ca (mm)
Water	72.0	997	0.89	2.7
Methanol	21.4	777	0.47	1.67
FC-72	12.0	1680	0.64	0.79
<i>n</i> -Hexane	18.4	600	0.30	1.68

wick heat pipe and confirmed that the use of the Kozeny–Carman expression resulted in a considerable error while the best agreement was found using the Forchheimer model. The Kozeny-like model, taking into account inertial effects is updated in terms of constant values, which fit with experimental data very well.

4.2. Capillary rate-of-rise test

In this subsection, the results of capillary rate-of-rise tests according to w - t and h - t techniques are presented. Water, methanol, *n*-Hexane and FC-72 are used for the w - t technique and *n*-Hexane and methanol are used for the h - t technique. The properties of tested fluids are presented in Table 4. It should be noted that to obtain the real wicking mass, the de-wetting mass in attachment of an outer meniscus to the wick is subtracted from the mass raw data, as the initial jump in mass refers to both the wetting and wicking process.

4.2.1. Capillary rate-of-rise test: w - t technique versus h - t technique

Fig. 9 shows a sequence of IR thermal images of capillary rise in which the liquid front is registered and the capillary rise height is obtained. Fig. 10 shows the influence of the working fluid selection on the capillary uptake rate for the w - t technique as well as the ratio of rise of mass to its maximum mass over time. Fig. 10(a) shows that when the wick sample is brought into contact with the working fluids, the working fluids all rise very quickly at the early stage of the capillary rising process. It is obvious that the mass rate decreases with time. Fig. 10(b) shows that water, FC-72, *n*-Hexane and methanol reach 90% of equilibrium at 6, 6.6, 14 and 20 s, respectively. High velocity in the capillary pumping stage is due to the large permeability of the wick sample and the fact that the friction resistance of the working fluid flow is small, both resulting in a fast rise of fluid. From the driving force point of view, capillary pumping is associated with the surface tension of the working fluid: the larger the surface tension, the larger the capillary pumping. On the other hand, from the resistance aspect, a smaller liquid viscosity and larger density, result in smaller friction resistance when liquid passes through the porous media. Comparing FC-72, *n*-Hexane and methanol: the viscosity of FC-72 is higher than *n*-Hexane and methanol; however, its density is more than two times that of *n*-Hexane and methanol. Large capillary pumping is likely due to higher density. Also comparing FC-72 and water: water has a larger surface tension and viscosity, showing higher capillary pumping.

A similar observation is obtained from the h - t technique. Fig. 11 shows the capillary rate-of-rise height as a function of time for two types of fluids: *n*-Hexane and methanol. Both have a similar theoretical capillary length, $(\sigma/\rho g)^{1/2}$, 1.67 mm for methanol and 1.68 mm for *n*-Hexane, *n*-Hexane however has smaller viscosity. Moreover, *n*-Hexane features a near zero contact angle with respect to the wick material. When the sample first makes contact with the liquid, a rapid rise can be seen. This is due to fact that the capillary force is much larger than the flow resistance and the gravity effect, so the wetted height in the wick shows a fast rising velocity. After the initial stage, the capillary rise of liquid in the sample slows down for both fluids similar to that of the w - t technique. Despite these fluids having a similar theoretical capillary length, *n*-Hexane exhibits a quicker capillary rise. This may result from the fact that *n*-Hexane has a smaller viscosity than

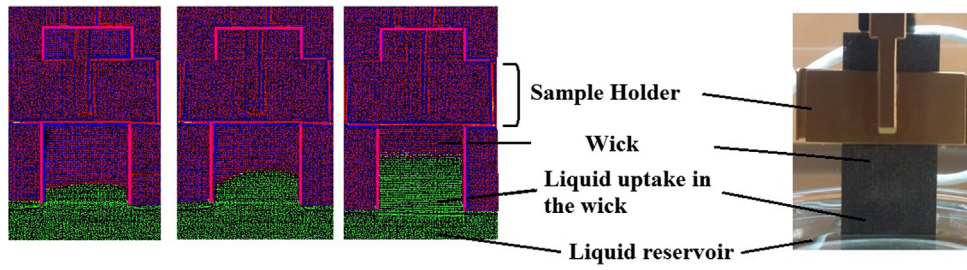


Fig. 9. Example of IR images of capillary rise during the capillary rise test.

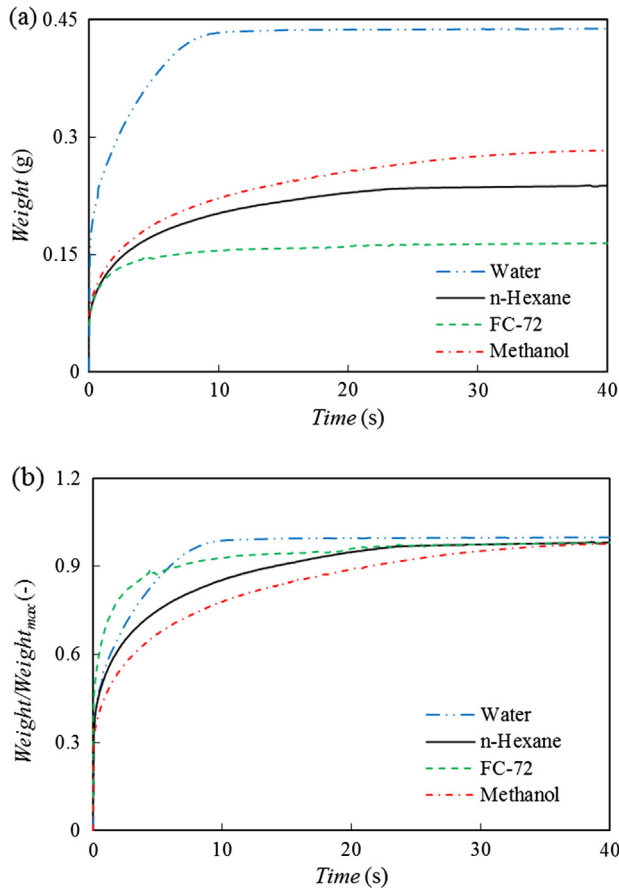


Fig. 10. Liquid mass increase in porous structure as a function of time (a) and ratio of mass rise to maximum mass over time for different working fluid (b).

methanol. Based on the h - t technique, the 90% of equilibrium height is obtained at 12.9 and 18.8 s for n -Hexane and methanol, respectively. This shows a relatively good agreement between equilibrium rise based on height and mass techniques, mentioned above, 14 and 20 s, respectively. The equilibrium height for a grooved wick with acetone as working fluid was reported at 10 s [9] while for a sintered porous wick with ethanol as working fluid failed to reach the equilibrium height even after 120 s [56]. The capillary pumping results of the 3D-printed wick are comparable to grooved wick structures while a better capillary pumping compared to sintered wicks is obtained due to lower flow resistance.

4.2.2. Capillary rise dynamic evaluation

In order to characterize the capillary rise dynamics of the 3D-printed wick, the presented data from w - t technique according to Fig. 10 are normalized in Fig. 12, as $h/a \sim (\sigma t/\mu a)^{1/3}$ curves. It can be seen that the experimental results in the intermediate stage approximately 1–6 s of the capillary rise processes can be very well fitted by

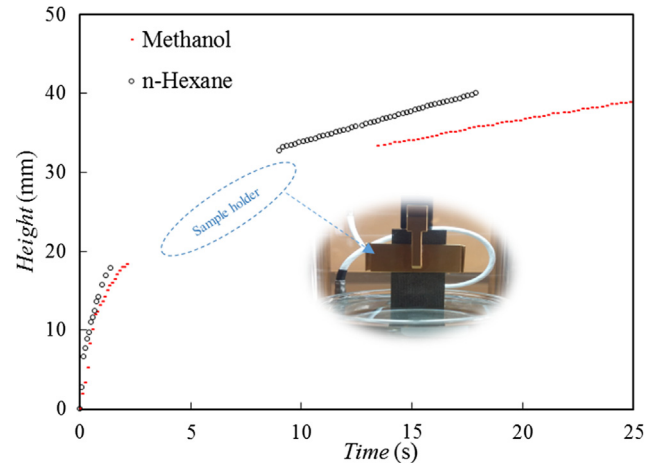


Fig. 11. Liquid height increase in porous structure as a function of time for n -Hexane and methanol. The gap in recording height is due to the sample holder.

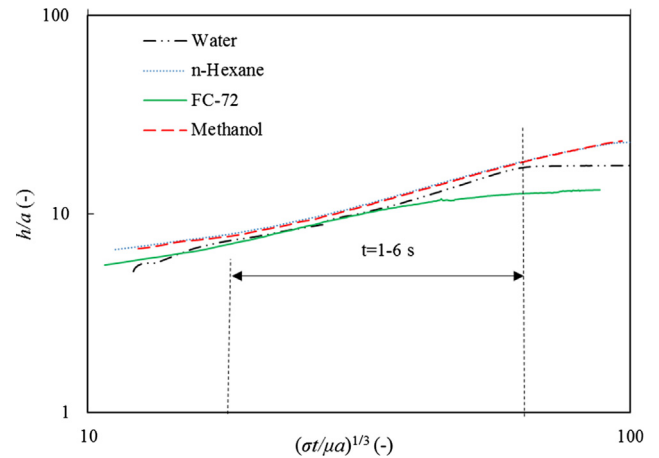


Fig. 12. Evolution of capillary rise dynamic as a function of $h/a \sim (\sigma t/\mu a)^{1/3}$ for different working fluid. The equilibrium height is obtained based on w - t experiments.

linear curves, as predicted by (10), except for FC-72 in which case 1–3 s is used for curve fitting. This is likely due to fact that FC-72 shows high capillary rise compared to other fluids and the equilibrium height for water, n -Hexane and methanol is up to the top edge of the sample, however, for FC-72 the top is almost 20% of the sample height, remarking the effect of gravity as FC-72 has the largest density.

The capillary penetration the sample can be well governed by $h(t) \sim t^{1/3}$. The deviations of the linear fitting are found to be as 2.8%, 2.6%, 5.5% and 1.5% for water, n -Hexane, FC-72 and methanol, respectively. This behaviour differs significantly from the classic Washburn expression $h(t) \sim t^{1/2}$. There is a small gap between the curves for all working fluids in which they do not collapse very well in a single line; however, they have a similar slope as evidenced in Table 5. Different findings

Table 5

Fitting parameters according to Fig. 12 for capillary rise expression of $h/a \sim (\sigma t/\mu a)^{1/3}$.

Fluid	Slope	Error (%)
Water	0.235	2.8
Methanol	0.245	1.5
FC-72	0.211	5.5
<i>n</i> -Hexane	0.244	2.6

available in the literature applying the $h(t) \sim t^{1/3}$ -expression. Previous studies showed that the curves can be collapsed in a single line using different geometries [61,75] or there is a gap between the curves as well as different slopes using different wicks and working fluids [62]. A reason for the discrepancy of results attributes to different contact angles formed between wick material and different working fluids, which is not taken into account by this model since complete wetting is assumed. However, we observe that the difference of the contact angle between different liquids and wick material is negligible on the capillary penetration at the intermediate stage. As evidenced from Fig. 12, except for the aforementioned period of capillary rise, the deviations from linear fitting are observed in the long-time stage (approximately after 6 s for water, methanol and *n*-Hexane and after 3 s for FC-72). Besides, Fig. 12 shows that in the long time stage, the rising velocity decreases due to the increasing gravitational resistance. The capillary rising cannot follow the $h/a \sim (\sigma/\mu a)^{1/3}$ expression anymore. To characterize the initial stage 0.2–1 s, first, we evaluated the validity of the simplified Washburn expression (11) to characterize the capillary rate-of-rise for the selected set of working fluids: $h^2 \sim \text{time}$ and $m^2 \sim \text{versus time}$. A regime that corresponds to the phenomenon leading to the Washburn results, i.e., a regime in which inertia and gravity may be neglected, was not identified. Therefore, this model is not accurate for our system. This is likely because of the large pore size. As reported in the literature the application of Washburn's equation is more suited for pore sizes ($< 150 \mu\text{m}$) [50], while in this study pore sizes are almost $216 \mu\text{m}$.

It is concluded the working fluid shows negligible effects on the $h(t) \sim t^{1/3}$ - expression in the intermediate stage of capillary rise, whereas it plays an important role on the initial and long-time stage. Observation confirms that the gravitational effect played a significant role in the 3D-printed wick, introducing slower capillary rising. Therefore, in the following section the effect of gravity is considered in the capillary performance evaluation.

4.2.3. Capillary performance evaluation in terms of K/r_{eff}

Based on (10) which includes the effect of gravity, the relation between dm/dt and $1/m$, and corresponding dh/dt and $1/h$, are evaluated to compute the linear fitting. It is found that for all tests, the linear fit matched the early stages of rising accurately. The corresponding capillary performance parameters are listed in Table 6. The maximum relative deviation of K/r_{eff} for the different fluids included in our study was about 12.6% for *w-t* technique and 16% for *h-t* technique. Since the parameter K/r_{eff} characterizes the capillary performance of wicks without considering the surface tension of the working liquid, this parameter should be nearly

Table 6

Capillary performance measurement with regard to dm/dt and $1/m$ and dh/dt and $1/h$.

	<i>w-t</i> test	<i>h-t</i> test	Relative deviation of K/r_{eff} for <i>w-t</i> and <i>h-t</i> tests
	K/r_{eff} (μm)	K/r_{eff} (μm)	
Water	1.044	–	
Methanol	1.078	1.18	6.5%
<i>n</i> -Hexane	0.84	0.93	7.5%
FC-72	0.939	–	

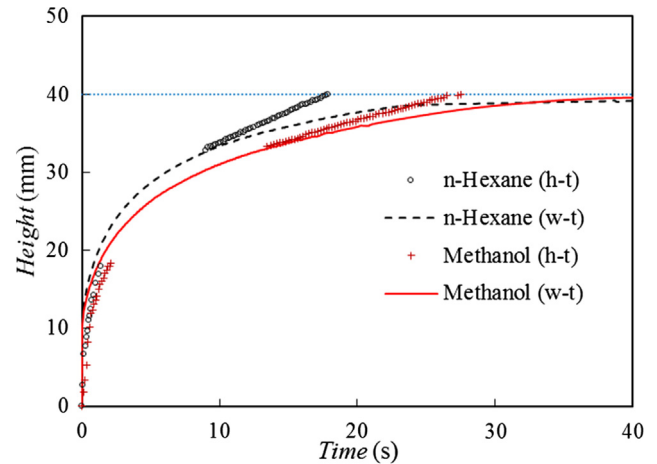


Fig. 13. Comparison of equilibrium height obtained based on *h-t* and *w-t* techniques.

constant. A reason may be the different contact angles formed between the working liquids and the wick material: a lower contact angle decreases the effective pore radius. The contact angle is not taken into account in the applied correlation. As described in Section 4.2.2, the difference in contact angle between different liquids and wick material is negligible on the capillary penetration in the intermediate stage; however, it was shown that the difference in contact angle plays an important role on the initial stage of capillary rising.

In order to show that the results of the *w-t* and *h-t* techniques are equivalent, the capillary performance obtained from both techniques is summarized in Table 6 as well. As evidenced, K/r_{eff} obtained from the *w-t* technique is comparable but slightly lower than obtained from the *h-t* technique for both methanol and *n*-Hexane. The relative deviation of K/r_{eff} for *w-t* and *h-t* tests is as high as 6.5% and 7.5% for methanol and *n*-Hexane, respectively. Such differences can be attributed to experimental parameters and noise. Moreover, another reason could be due to fact that the pores with the larger diameter fill more quickly. Fluid uptake by the larger pores is observed with the *h-t* technique, whereas penetration into smaller pores at the same height occurs later. This is confirmed in Fig. 13 in which the equilibrium height based on *w-t* and *h-t* techniques is shown. The equilibrium height is observed at 18 s and 27.5 s for *n*-Hexane and methanol based on *h-t* technique while 45 s and 48 s based on *w-t* technique, respectively. We can conclude that despite there is a difference between computed mass and height rises over time, measurement of both experimental techniques are equivalent at early stage of operation to characterize the capillary performance of 3D-printed wicks, as the relative deviation error is 6.5–7.5%.

From capillary rate-of-rise-tests, it is concluded that the capillary penetration of liquids in the 3D-printed wick follows the expression: $h(t)/a \sim (\sigma t/\mu a)^{1/3}$ at intermediate stage. Different working fluids show negligible effect in the intermediate stage; however, they do play an important role in the initial stage of capillary rising. Results from this study can be applied for relatively large pore sizes, however, to examine dependences between pore size and size distribution, a systematically 3D-printed porous structure with different pore sizes is suggested. It is also concluded that the capillary performance of a 3D-printed wick structure should be determined by integrating the gravity effect. The well-known Washburn's equation cannot characterize the capillary rate-of-rise processes, as a linear match was not observed. Similar results are obtained by [56], which tested a sintered porous structure with different particle sizes (< 50 , 50–75, 75–110 and 110–150 μm).

4.3. Performance of the fabricated porous structure for two-phase devices

In this section, we compare the wick properties, effective pore

Table 7

Wick properties for comparison from current and previous studies as well as capillary performance results.

Type of wicks	ε (–)	K ($\times 10^{-11} \text{ m}^2$)	K/r_{eff} (μm)
Current study, 3D-printed (500 μm unit cell size; $D = 216 \mu\text{m}$)	0.46	13.05	1.04
3D-printed (300 μm unit cell size; $D = 120 \mu\text{m}$) [34]	0.17	0.027	0.02
3D-printed (500 μm unit cell size; $D = 280 \mu\text{m}$) [34]	0.58	27	7.14
Composite, spherical powder [56]	0.57	0.183	0.15
Composite, irregular powder [56]	0.57	0.383	0.43
Sintered, spherical powder [56]	0.57	0.475	0.46
Sintered, irregular powder [56]	0.57	0.671	0.60
Sintered, spherical powder [37]	0.28	0.24	0.19
Sintered, spherical powder [38]	0.43	1.79	0.39
Sintered, spherical powder [39]	0.56	0.36	0.22
Sintered [76]	0.36	1.27	0.254
Grooved [56]	0.50	49.2	12.90
Monel beads mesh (140–200) [14]	0.40	1.10	0.25
Metallic weave [63]	0.24	3.60	0.05

radius and capillary performance of the 3D-printed wick structure with other porous structures for heat pipe applications reported in the literature, shown in Table 7. In this light, K/r_{eff} is used to evaluate the capillary performance of wick structures. It is shown that \sqrt{K} is smaller than the effective pore radius with an approximate order of magnitude $10^{-2}r_{\text{eff}}$ for sintered metal wicks, $10^{-1}r_{\text{eff}}$ for grooved wicks and $10^{-3}r_{\text{eff}}$ for screen mesh wicks. The 3D-printed wick of this study showed comparable and the same order of magnitude to that of screen mesh wicks $10^{-3}r_{\text{eff}}$ while showing around 4 times greater capillary performance. As shown in Table 7, the capillary performance parameter (K/r_{eff}) of the 3D-printed wick in this study is 1–6 times greater larger than that of sintered and composite porous structure. This is due to the larger permeability and smaller friction resistance. Compared to the grooved wick structure, the 3D-printed wick of this study shows two order of magnitudes lower capillary performance, due to large permeability of grooved wicks.

Due to a lack of research on additively manufactured porous structures for heat pipe applications, little data was available to compare the presented experimental data of the current study with other 3D-printed wick structures [33,34]. Ameli et al. [34], e.g., showed a relatively similar permeability of $1.12\text{--}1.52 \times 10^{-10} \text{ m}^2$ for a 3D-printed wick structure with nearly identical spherical powder size and unit cell size. Esarte et al. [33] tested a 3D-printed wick with lower pore sizes, ranging between 70 and 90 μm , and showed lower values of permeability around $1.25 \times 10^{-12} \text{ m}^2$. They showed that after 1 s using methanol as working fluid a height rise of around 19 mm. We observed a relatively equal height rise (about 18.5 mm) with a porous structure having higher pore size. From this comparison, it can be concluded that apart from the pore size of additively manufactured porous structures, a sinter-style layer formed on the surface of the wick and feature size can influence its capillary performance.

In summary, it can be concluded that because of its large permeability and K/r_{eff} , the performance in conjunction with a 3D-printed wick can significantly augment heat transfer. Moreover, the 3D-printing process allows for fabricating of the wick structure in a non-uniform way. 3D-printed wicks appear to be a promising alternative to standard wicks for heat pipes: the example discussed in this paper shows higher capillary performance compared to sintered wicks, by which it increases the capillary limit of heat pipes.

5. Conclusions

This work examined the wicking behaviour of a 3D-printed stainless steel porous structure. Key design parameters of porous structures for

heat pipe applications were discussed including porosity (ε), permeability (K), effective pore radius (r_{eff}) capillary pumping head (h), capillary pumping mass (m) and capillary performance (K/r_{eff}). These and other quantities were investigated experimentally, highlighting the role of the working fluid. Permeability of the wick was determined by forced liquid flow tests. The capillary pumping performance of the wick was characterized by capillary rate-of-rise experiments using w - t and h - t techniques. The main conclusions can be listed as follows:

- It was found that the transition regime between the linear Darcy regime and when drag becomes important for the tested sample occurs in a Re_K of 0.95 which corresponds to a flow velocity of 0.07 m/s based on the permeability and form coefficient in this range.
- The measured permeability, according to Darcy's law, was found to be in close agreement at low liquid velocities (up to 0.07 m/s) with predictions considering Kozeny–Carman correlation with a C value of 122. The Kozeny-like model, taking into account inertial effects, is updated in terms of constant values, which fit with experimental data very well for both low and high velocities.
- Observation confirms that the gravitational effect, introducing slower capillary rising, played a significant role in the 3D-printed wick. The well-known Washburn's equation ($h \sim t^{1/2}$) cannot characterize the capillary rate-of-rise processes.
- The capillary rise dynamics of the 3D-printed wick was evaluated for different working fluids in terms of $h/a \sim (\sigma/\mu a)^{1/3}$ curves. It was concluded that the working fluid shows negligible effects on the $h(t) \sim t^{1/3}$ – law in the intermediate stage of capillary rise, whereas it plays an important role on the initial and long-time stage.
- The SLM-fabricated wick of this study was compared to literature wick properties. It is concluded that due to large permeability and K/r_{eff} of the 3D-printed wick, the performance of a 3D-printed heat pipe can significantly augment heat transfer.

In conclusion, the present study establishes a range of experimental methods with which the capillary performance of a 3D-printed porous structure can be quantified reliably. Moreover, the validity of theoretical predictions of single-phase properties was put in perspective.

Acknowledgement

This research was supported by the Science Based Engineering (SBE) program of the University of Twente.

References

- [1] D. Jafari, et al., Two-phase closed thermosyphons: a review of studies and solar applications, *Renew. Sustain. Energy Rev.* 53 (Suppl. C) (2016) 575–593.
- [2] W.W. Wits, G.J. te Riele, Modelling and performance of heat pipes with long evaporator sections, *Heat Mass Transfer* 53 (11) (2017) 3341–3351.
- [3] W.W. Wits, T.H.J. Vaneker, Integrated design and manufacturing of flat miniature heat pipes using printed circuit board technology, *IEEE Trans. Compon. Packag. Technol.* 33 (2) (2010) 398–408.
- [4] W. Wits et al., Thermal management through in-board heat pipes manufactured using printed circuit board multilayer technology, in: 2006 Thirty-First IEEE/CPMT International Electronics Manufacturing Technology Symposium, 2006.
- [5] D. Jafari, et al., An experimental investigation on the evaporation and condensation heat transfer of two-phase closed thermosyphons, *Exp. Therm. Fluid Sci.* 88 (2017) 111–123.
- [6] A. Faghri, *Heat Pipe Science and Technology*, Taylor & Francis, Philadelphia, PA, 1995.
- [7] P.D. Marco, et al., Theoretical analysis of screened heat pipes for medium and high temperature solar applications, *J. Phys. Conf. Ser.* 547 (1) (2014) 012010.
- [8] W.W. Wits, J.H. Mannak, R. Legtenberg, Selecting capillary structures for heat pipes in multilayer printed circuit boards, in: 5th European Thermal Sciences Conference, Eindhoven, The Netherlands, 2008.
- [9] G. Huang, et al., Enhanced capillary performance in axially grooved aluminium wicks by alkaline corrosion treatment, *Exp. Therm. Fluid Sci.* 82 (2017) 212–221.
- [10] J. Cheng, et al., Enhancement of capillary and thermal performance of grooved copper heat pipe by gradient wettability surface, *Int. J. Heat Mass Transfer* 107 (2017) 586–591.

- [11] D. Jafari, et al., An experimental investigation and optimization of screen mesh heat pipes for low-mid temperature applications, *Exp. Therm. Fluid Sci.* 84 (2017) 120–133.
- [12] J.A. Weibel, S.V. Garimella, M.T. North, Characterization of evaporation and boiling from sintered powder wicks fed by capillary action, *Int. J. Heat Mass Transfer* 53 (19–20) (2010) 4204–4215.
- [13] K. De Kerpel, et al., Experimental study of the effect of felt wick porosity on capillary-driven heat pipes, *Appl. Therm. Eng.* 96 (2016) 690–698.
- [14] A. Faghri, *Heat Pipe Science and Technology*, Taylor & Francis Group, Washington, DC, 1996.
- [15] D.A. Reay, P.A. Kew, *Heat Pipes* (2006) ix.
- [16] G. Peterson, *An Introduction to Heat Pipes: Modeling, Testing, and Applications*, John Wiley and Sons, 1994.
- [17] F. Lefèvre, et al., Experimental investigations of flat plate heat pipes with screen meshes or grooves covered with screen meshes as capillary structure, *Appl. Therm. Eng.* 37 (2012) 95–102.
- [18] K.V. Paiva, M.B.H. Mantelli, Wire-plate and sintered hybrid heat pipes: Model and experiments, *Int. J. Therm. Sci.* 93 (2015) 36–51.
- [19] J. Wang, I. Catton, Enhanced evaporation heat transfer in triangular grooves covered with a thin fine porous layer, *Appl. Therm. Eng.* 21 (17) (2001) 1721–1737.
- [20] G. Franchi, X. Huang, Development of composite wicks for heat pipe performance enhancement, *Heat Transfer Eng.* 29 (10) (2008) 873–884.
- [21] X. Huang, G. Franchi, Design and fabrication of hybrid bi-modal wick structure for heat pipe application, *J. Porous Mater.* 15 (6) (2008) 635–642.
- [22] C.C. Yeh, C.N. Chen, Y.M. Chen, Heat transfer analysis of a loop heat pipe with biporous wicks, *Int. J. Heat Mass Transfer* 52 (19–20) (2009) 4426–4434.
- [23] X.B. Ji, et al., Pool boiling heat transfer on uniform and non-uniform porous coating surfaces, *Exp. Therm. Fluid Sci.* 48 (2013) 198–212.
- [24] G.S. Hwang, et al., Modulated wick heat pipe, *Int. J. Heat Mass Transfer* 50 (7–8) (2007) 1420–1434.
- [25] L.L. Jiang, et al., Thermal performance of a novel porous crack composite wick heat pipe, *Energy Convers. Manage.* 81 (2014) 10–18.
- [26] W.S. Ling, et al., Thermal performance of loop heat pipe with porous copper fiber sintered sheet as wick structure, *Appl. Therm. Eng.* 108 (2016) 251–260.
- [27] Y. Li, H.-F. He, Z.-X. Zeng, Evaporation and condensation heat transfer in a heat pipe with a sintered-grooved composite wick, *Appl. Therm. Eng.* 50 (1) (2013) 342–351.
- [28] M.P. Zwier, W.W. Wits, Design for additive manufacturing: automated build orientation selection and optimization, *Proc. CIRP* 55 (2016) 128–133.
- [29] Y. Zhang, et al., Additive manufacturing of metallic materials: a review, *J. Mater. Eng. Perform.* 27 (1) (2018).
- [30] D.A. Ramirez, et al., Open-cellular copper structures fabricated by additive manufacturing using electron beam melting, *Mater. Sci. Eng. A* 528 (16) (2011) 5379–5386.
- [31] G.P. Manogharan, Analysis of Non-Stochastic Lattice Structure Design for Heat Exchanger Applications, MS Thesis North Carolina State University, Raleigh, 2009.
- [32] D. Jafari, W.W. Wits, The utilization of selective laser melting technology on heat transfer devices for thermal energy conversion applications: a review, *Renew. Sustain. Energy Rev.* 91 (2018) 420–442.
- [33] J. Esarte, et al., Optimizing the design of a two-phase cooling system loop heat pipe: wick manufacturing with the 3D selective laser melting printing technique and prototype testing, *Appl. Therm. Eng.* 111 (Suppl. C) (2017) 407–419.
- [34] M. Ameli, et al., A novel method for manufacturing sintered aluminium heat pipes (SAHP), *Appl. Therm. Eng.* 52 (2) (2013) 498–504.
- [35] D. Jafari, W.W. Wits, B.J. Geurts, An investigation of porous structure characteristics of heat pipes made by additive manufacturing, in: *23rd International Workshop on Thermal Investigations of ICs and Systems*, Amsterdam, Netherlands, 2017, pp. 1–7.
- [36] D.A. Pruzan, et al., Design of high-performance sintered-wick heat pipes, *Int. J. Heat Mass Transfer* 34 (6) (1991) 1417–1427.
- [37] T. Semenic, Y.Y. Lin, I. Catton, Thermophysical properties of biporous heat pipe evaporators, *J. Heat Transfer-Trans. ASME* 130 (2) (2008).
- [38] R. Singh, A. Akbarzadeh, M. Mochizuki, Effect of wick characteristics on the thermal performance of the miniature loop heat pipe, *J. Heat Transfer-Trans. ASME* 131 (8) (2009).
- [39] F.A.D. Espinosa, T.B. Peters, J.G. Brisson, Effect of fabrication parameters on the thermophysical properties of sintered wicks for heat pipe applications, *Int. J. Heat Mass Transfer* 55 (25–26) (2012) 7471–7486.
- [40] K.S. Yang, et al., A novel oxidized composite braided wires wick structure applicable for ultra-thin flattened heat pipes, *Int. Commun. Heat Mass Transfer* 88 (2017) 84–90.
- [41] W. Ling, et al., Capillary pumping performance of porous copper fiber sintered wicks for loop heat pipes, *Appl. Therm. Eng.* 129 (2018) 1582–1594.
- [42] Y. Tang, et al., Effect of fabrication parameters on capillary performance of composite wicks for two-phase heat transfer devices, *Energy Convers. Manage.* 66 (2013) 66–76.
- [43] B. Holley, A. Faghri, Permeability and effective pore radius measurements for heat pipe and fuel cell applications, *Appl. Therm. Eng.* 26 (4) (2006) 448–462.
- [44] K. Boomsma, D. Poulikakos, The effects of compression and pore size variations on the liquid flow characteristics in metal foams, *J. Fluids Eng.* 124 (1) (2001) 263–272.
- [45] A.V. Kuznetsov, Analytical study of fluid flow and heat transfer during forced convection in a composite channel partly filled with a Brinkman-Forchheimer porous medium, *Flow, Turbulence and Combustion* 60 (2) (1998) 173–192.
- [46] G. Carbajal, C.B. Sobhan, G.P. Peterson, Dimensionless governing equations for vapor and liquid flow analysis of heat pipes, *J. Thermophys. Heat Transfer* 20 (1) (2006) 140–144.
- [47] D.A. Nield, A. Bejan, *Convection in Porous Media*, third ed., Springer, New York, 2006, p. xxiii 640 p.
- [48] C. Byon, S.J. Kim, Capillary performance of bi-porous sintered metal wicks, *Int. J. Heat Mass Transfer* 55 (15–16) (2012) 4096–4103.
- [49] E.W. Washburn, The dynamics of capillary flow, *Phys. Rev.* 17 (3) (1921) 273–283.
- [50] T. Dang-Vu, J. Hupka, Characterization of porous materials by capillary rise method, *Physicochem. Prob. Min. Process.* 39 (2005) 47–65.
- [51] J. Tian, et al., Capillary driven low-cost V-groove microfluidic device with high sample transport efficiency, *Lab Chip* 10 (17) (2010) 2258–2264.
- [52] R.R. Rye, J.A. Mann, F.G. Yost, The flow of liquids in surface grooves, *Langmuir* 12 (2) (1996) 555–565.
- [53] S. Cho, R. Tummala, Y. Joshi, Capillary performance of micropillar arrays in different arrangements, *Nanoscale Microscale Thermophys. Eng.* (2018) 1–17.
- [54] J.I. Siddique, D.M. Anderson, A. Bondarev, Capillary rise of a liquid into a deformable porous material, *Phys. Fluids* 21 (1) (2009) 013106.
- [55] A. Siebold, et al., Capillary rise for thermodynamic characterization of solid particle surface, *J. Colloid Interface Sci.* 186 (1) (1997) 60–70.
- [56] D.X. Deng, et al., Characterization of capillary performance of composite wicks for two-phase heat transfer devices, *Int. J. Heat Mass Transfer* 56 (1–2) (2013) 283–293.
- [57] L. Labajos-Broncano, et al., Comparison of the use of Washburn's equation in the distance-time and weight-time imbibition techniques, *J. Colloid Interface Sci.* 233 (2) (2001) 356–360.
- [58] L. Labajos-Broncano, M.L. González-Martín, J.M. Bruque, On the evaluation of the surface free energy of porous and powdered solids from imbibition experiments: equivalence between height-time and weight-time techniques, *J. Colloid Interface Sci.* 262 (1) (2003) 171–178.
- [59] D. Georgiou, E.P. Kalogianni, Height-time and weight-time approach in capillary penetration: investigation of similarities and differences, *J. Colloid Interface Sci.* 495 (2017) 149–156.
- [60] A. Alghunaim, S. Kirdponpattara, B.-M.Z. Newby, Techniques for determining contact angle and wettability of powders, *Powder Technol.* 287 (Suppl. C) (2016) 201–215.
- [61] A. Ponomarenko, D. Quéré, C. Clanet, A universal law for capillary rise in corners, *J. Fluid Mech.* 666 (2011) 146–154.
- [62] D. Deng, et al., Characterization of capillary rise dynamics in parallel micro V-grooves, *Int. J. Heat Mass Transfer* 77 (2014) 311–320.
- [63] N. Fries, et al., The effect of evaporation on the wicking of liquids into a metallic weave, *J. Colloid Interface Sci.* 321 (1) (2008) 118–129.
- [64] C. Byon, S.J. Kim, The effect of meniscus on the permeability of micro-post arrays, *J. Micromech. Microeng.* 21 (11) (2011).
- [65] D. Georgiou, et al., Capillary penetration in cellulose and polyethylene porous media: effect of contact with vapours and partial saturation with a non-miscible liquid, *Colloids Surf. A: Physicochem. Eng. Asp.* 483 (2015) 297–306.
- [66] G.S. Hwang, et al., Multi-artery heat pipe spreader: experiment, *Int. J. Heat Mass Transfer* 53 (13–14) (2010) 2662–2669.
- [67] C. Ravey, E. Ruiz, F. Trochu, Determination of the optimal impregnation velocity in Resin Transfer Molding by capillary rise experiments and infrared thermography, *Compos. Sci. Technol.* 99 (2014) 96–102.
- [68] A. Rabbani, S. Jamshidi, S. Salehi, An automated simple algorithm for realistic pore network extraction from micro-tomography images, *J. Petrol. Sci. Eng.* 123 (2014) 164–171.
- [69] D.A. Reay, P.A. Kew, *Heat Pipes, Theory, Design and Applications*, fifth ed., Butterworth-Heinemann, Oxford, 2006.
- [70] J.R. Taylor, *An Introduction to Error Analysis*, second ed., University Science Book, US, 1997.
- [71] B. Eisefeld, K. Schnitzlein, The influence of confining walls on the pressure drop in packed beds, *Chem. Eng. Sci.* 56 (14) (2001) 4321–4329.
- [72] M. Kaviany, *Principles of Heat Transfer in Porous Media*, Springer-Verlag, New York, 1991.
- [73] X. Huang, G. Franchi, F. Cai, Characterization of porous bi-modal Ni structures, *J. Porous Mater.* 16 (2) (2009) 165–173.
- [74] J.-P. Bonnet, F. Topin, L. Tadrist, Flow laws in metal foams: compressibility and pore size effects, *Transp. Porous Media* 73 (2) (2008) 233–254.
- [75] N. Obara, K. Okumura, Imbibition of a textured surface decorated by short pillars with rounded edges, *Phys. Rev. E* 86 (2) (2012) 020601.
- [76] J. Choi, et al., Experimental investigation on sintered porous wicks for miniature loop heat pipe applications, *Exp. Therm. Fluid Sci.* 51 (2013) 271–278.